EDGE ARTICLE

Check for updates

Azetidinyl Malachite Green: a superior fluorogen-activating protein probe for live-cell and dynamic SIM imaging†

Fei Deng, ‡[abc] Xiangning Fang,‡[ae] Qinglong Qiao,*[a] Guoli Han,[ae] Lu Miao,[a] Shuangshuang Long[ad] and Zhaochao Xu [*ae]

Malachite Green (MG) and its fluorogen-activating protein (FAP) pair are valuable tools for live-cell and super-resolution fluorescence imaging due to their unique near-infrared absorption and signal enhancement. However, the low brightness and photostability of MG have limited its use in dynamic imaging. In this study, we introduce a novel derivative, azetidinly Malachite Green (**Aze-MG**), which enhances the brightness of the MG-FAP complex by 2.6-fold. This enhancement is achieved by replacing the *N,N*-dimethylamino group in MG with an azetidine group, which suppresses the twisted intramolecular charge transfer (TICT) effect, leading to improved quantum yield and photostability. Additionally, the reduced binding affinity of **Aze-MG** for FAP enables a buffering strategy, allowing the reversible exchange of photobleached fluorogens with free fluorogens, thereby ensuring stable fluorescence over time. This combination of improved brightness and buffering capability makes **Aze-MG** an ideal probe for live-cell and dynamic SIM imaging.

Introduction

Long-term live-cell super-resolution fluorescence imaging is critical for uncovering the dynamic behaviors of cellular nanostructures.[1–3] Achieving this level of imaging requires fluorescent probes that offer high specificity, minimal background fluorescence, sufficient brightness, and photostability.[4–8] Despite significant advancements in dye chemistry and imaging techniques, designing probes that meet all these criteria remains a challenge.[9–13] Fluorogen-activating proteins (FAPs) have emerged as a promising solution for specific and high-contrast labeling in live cells.[14–18] These genetically encoded proteins bind to non-fluorescent fluorogens, resulting in significant fluorescence activation, which allows for high signal-to-noise imaging. Malachite Green (MG) and its FAP pair have been widely used due to their unique near-infrared absorption and strong signal enhancement. Waggoner

et al. pioneered this system by screening human single-chain antibodies to identify an MG-binding FAP, establishing its foundation in live-cell imaging.[19] This FAP encapsulates MG within its binding cavity, constraining the internal rotation of MG's aromatic rings and thereby suppressing non-radiative decay pathways. This interaction results in an 18 000-fold fluorescence increase in the near-infrared region, ideal for deep tissue imaging due to reduced background and scattering. Building on this work, Waggoner and Bruchez modified MG's pendent ring by introducing extended conjugation and primary amino groups,[20,21] creating MG derivatives that bind to the same FAP with emission maxima at 731 and 532 nm, respectively. Additionally, Hu *et al.* developed a series of 3-indole-MG derivatives exhibiting large "pseudo-Stokes" shifts upon binding to FAPs.[22] These studies demonstrate that FAPs exhibit good structural tolerance to modifications in MG, opening up opportunities for further structural modifications of MG. However, MG still faces significant limitations in brightness and photostability, which are critical for sustained dynamic super-resolution imaging.[23,24] It is prone to photobleaching and has a limited quantum yield, which complicates long-term super-resolution microscopy and stable tracking of cellular events. Thus, despite the value of MG-FAP pairs, maintaining stable fluorescence for extended imaging remains a major challenge.

A promising strategy to maintain stable fluorescence over time involves using a "buffering" approach, where fluorescent dyes can reversibly bind to their targets.[25] This allows free, non-fluorescent dyes in the surrounding environment to replace

[a] Dalian Institute of Chemical Physics, Chinese Academy of Sciences, 457 Zhongshan Road, Dalian 116023, China. E-mail: qqlqiao@dicp.ac.cn; zcxu@dicp.ac.cn

[b] School of Chemistry and Chemical Engineering, Jinggangshan University, 28 Xueyuan Road, Ji'an, Jiangxi 343009, China

[c] Key Laboratory of Jiangxi Province for Special Optoelectronic Artificial Crystal Materials, Jinggangshan University, 28 Xueyuan Road, Ji'an, Jiangxi 343009, China

[d] School of Chemistry and Chemical Engineering, University of South China, 28 Changshengxi Road, Hengyang, Hunan 421001, China

[e] University of Chinese Academy of Sciences, Beijing 100049, China

† Electronic supplementary information (ESI) available. See DOI: https://doi.org/10.1039/d5sc01150g

‡ These two authors contributed equally.

photobleached dyes on the target, sustaining a consistent imaging signal.[26] This reversible binding approach has been effectively applied in organelle imaging, where dyes bind in an interchangeable manner to the organelle membrane matrix.[27–29] Here, non-specific interactions are sufficient for binding, allowing for probe exchange simply by adjusting the hydrophilic or lipophilic properties of the dye to interact with the organelle membrane. However, designing reversible binding systems for biomolecule–substrate interactions poses greater challenges due to the specificity required. Unlike organelles, biomolecular targets rely on precise molecular recognition; even small structural changes in the dye can disrupt its binding affinity or specificity, making it difficult to achieve both strong binding and rapid exchange.

Rhodamine, which shares significant structural similarity with MG, offers insights into addressing MG's fluorescence limitations.[30] In rhodamine dyes, a major nonradiative de-excitation pathway is twisted intramolecular charge transfer (TICT), commonly originating from alkylamino substituents.[31,32] Studies show that non-alkylated rhodamine 110 and alkyl-substituted rhodamine 101 have quantum yields of 0.88 and 0.80, respectively, both considerably higher than that of tetramethylrhodamine (TMR) (0.41).[33] Notably, Lavis *et al.* found that replacing TMR's *N,N*-dimethyl groups with azetidine rings effectively suppressed TICT, doubling its quantum efficiency.[34] For MG, crystallographic studies of FAP-bound complexes reveal that the binding cavity is over twice the volume of MG itself.[35] While aromatic ring rotations are restricted in this environment, the *N,N*-dimethyl groups in MG remain capable of free rotation within the cavity, likely contributing to TICT-induced fluorescence quenching and reducing the overall quantum yield.

In this work, we address these limitations by engineering a novel derivative of **Aze-MG** (**MG3** in this paper) to enhance both brightness and dynamic imaging potential. Through strategic modification of MG's structure, specifically by introducing azetidine in place of the dimethylamino groups, we successfully increased the brightness of the MG-FAP complex by threefold. This modification suppresses the twisted intramolecular charge transfer (TICT) effect, resulting in improved quantum yield and photostability. Additionally, we implemented a buffering strategy that enables **Aze-MG** to reversibly bind with FAP, allowing free fluorogen molecules to replace photobleached ones at the target site. This exchangeable binding capacity supports stable fluorescence over time and enables continuous dynamic imaging under structured illumination microscopy (SIM).

Results and discussion

In alignment with the concept of TICT suppression, we synthesized three derivatives of MG (Fig. 1a)—**MG2** with an amino group, **MG3** with an azetidine group, and **MG4** with a julolidine group—replacing the *N,N*-dimethyl groups present in the control dye (**MG1**). The synthesis of **MG4** was achieved directly *via* the condensation of benzaldehyde with julolidine, similar to **MG1**. In contrast, **MG2** and **MG3** were synthesized
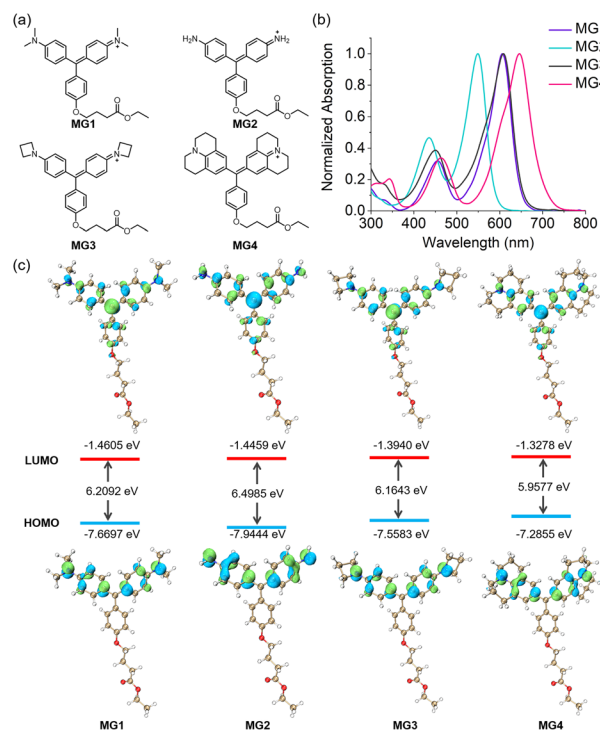

Fig. 1 (a) Molecular structures of **MG1–4**. (b) Absorption spectra of **MG1–4** in PBS (pH 7.40). (c) Computed frontier orbitals and energy levels of **MG1–4**.

from bisphenol compounds using Pd-catalyzed C–N cross-coupling reactions (Scheme S1†). We first investigated the intrinsic absorption and emission spectra of these **MG** derivatives. **MG3** and **MG1** shared almost the same absorption maximum at 606 nm whereas **MG2** and **MG4** were blue-shifted by 57 nm and red-shifted by 40 nm, respectively, compared to **MG1** (Fig. 1b). Notably, the fluorescence of **MG2–4** was almost completely quenched, likely due to intense vibrational deactivation (Fig. S2 and S3†), making it difficult to observe. We subsequently performed calculations for **MG1–4** using time-dependent density functional theory. It revealed that for all dyes, the lowest energy excitation was attributed solely to the HOMO–LUMO transition, with HOMO–LUMO gaps measured at 6.2092 eV for **MG1**, 6.4985 eV for **MG2**, 6.1643 eV for **MG3**, and 5.9577 eV for **MG4**, aligning with the observed trends in their absorption maxima (Fig. 1c).

Table 1 Photophysical properties of MGs and the MGs/dL5** complex

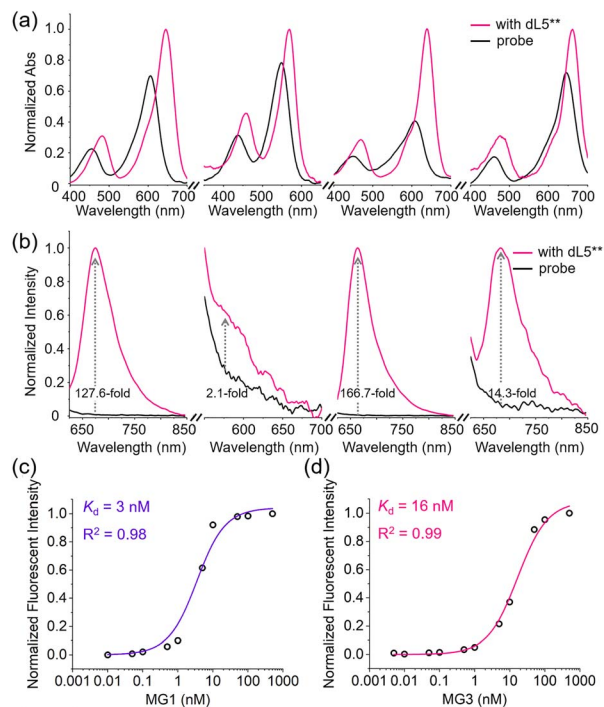| Dye	λ_{abs} (nm)	ε (M^{-1} cm^{-1})	λ_{em} (nm)	Φ	K_d (nM)
MG1	606	71 000	n.d.	n.d.	3
MG1/dL5**	646	102 000	675	0.12	—
MG2	549	31 000	n.d.	n.d.	n.d.
MG2/dL5**	569	39 000	n.d.	n.d.	—
MG3	607	43 000	n.d.	n.d.	16
MG3/dL5**	639	113 000	664	0.28	—
MG4	646	54 000	n.d.	n.d.	61
MG4/dL5**	661	75 000	684	0.04	—

Fig. 2 (a) Absorption and (b) fluorescence spectra of 0.5 μM MGs in the absence and presence of 2 μM dL5** (MG1–4: from left to right). Binding equilibrium analysis of MG1 (c) and MG3 (d) to dL5**.

Prior research identified dL5 as an ideal FAP to switch on the fluorescence of MG1.[36] We then evaluated the activating ability of dL5** to MG2–4. As presented in Table 1, the absorption maxima of all MGs red-shifted upon the addition of 4 fold excess of dL5**.[21,35] Specifically, MG2–4 were red-shifted by 20, 32 and 15 nm, respectively, which were much smaller than the 40 nm shift observed for MG1. The absorbance of each MG further increased upon binding with dL5**, with MG3 showing a remarkable 2.6-fold enhancement, significantly surpassing

the changes observed in the other derivatives (Fig. 2a). As anticipated, MG1 showed a fluorescence turn-on response to dL5** with a quantum yield of 0.12. Bruchez et al. attributed this phenomenon to the interactions between MG1 and residues located in both the complementarity-determining regions (CDRs) and framework regions of dL5**. Notably, the dimethylamine carbons of MG1 contribute approximately 50% of the total contact area, a feature critical for fluorescence enhancement by restricting intramolecular rotation.[35] The negligible fluorescence of MG2/dL5** in our study further supports these findings. The absence of dimethylamine carbons in MG2 results in reduced conformational constraints and a complete loss of fluorescence activation. While the azetidine carbons in MG3 exert a similar effect in the interactions. The MG3/dL5** fluoromodule emits fluorescence in the near-infrared region with a significantly higher quantum yield of 0.28, achieving a 166.7-fold fluorescence enhancement (Fig. 2b). Although MG4 contains julolidine carbons, its substantially larger molecular size likely weakens the binding interaction with dL5**, resulting in only 14.3-fold fluorescence enhancement with a quantum yield of 0.04 upon complex formation. The dissociation constants K_d of MGs to dL5** were measured using a ligand depletion assay at the emission maximum. The K_d values for MG1, MG3 and MG4 were determined to be 3, 16 and 61 nM, respectively (Fig. 2c, d and S4†), showing high affinity to dL5**.

To investigate the structure–fluorescence relationship of MG-based fluoromodules, we conducted docking simulations. The 3D structure of dL5** (D50E mutation) was constructed using homology modeling based on the MG1-bound L5* (PDB ID: 4K3H) as a template.[35] As shown in Fig. 3, the MG derivatives were positioned within the binding cavity formed by a symmetric antiparallel homodimer. MG2 and MG3 oriented approximately orthogonally to the dL5** surface, with their pendent rings extending outward from the cavity, consistent with the orientation observed in MG1. In contrast, MG4 was inserted into the binding cavity with its julolidine moiety
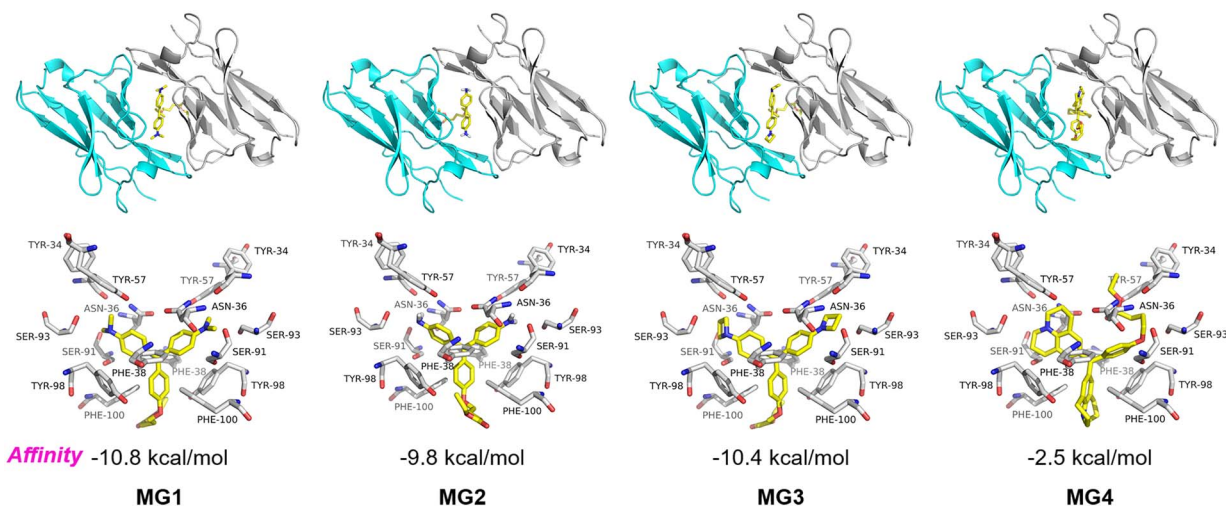

Fig. 3 Molecular docking analysis of MGs. (Top) Frontal view of the MGs/dL5** complex. (Bottom) Spatial distribution of amino acid side chains in dL5** that come in contact with MGs.

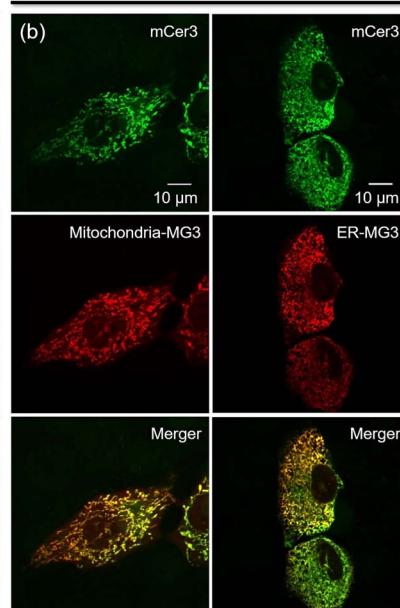protruding outside. The calculated binding affinities for **MG1–4** were −10.8, −9.8, −10.4, and −2.5 kcal mol^{-1}, respectively, indicating almost the same affinity for **MG1–3**. Although the results indicated that dL5** had a high affinity for **MG2**, fluorescence from the **MG2**/dL5** complex was not observed. This is likely because the crystal structure of 4K3H revealed that the
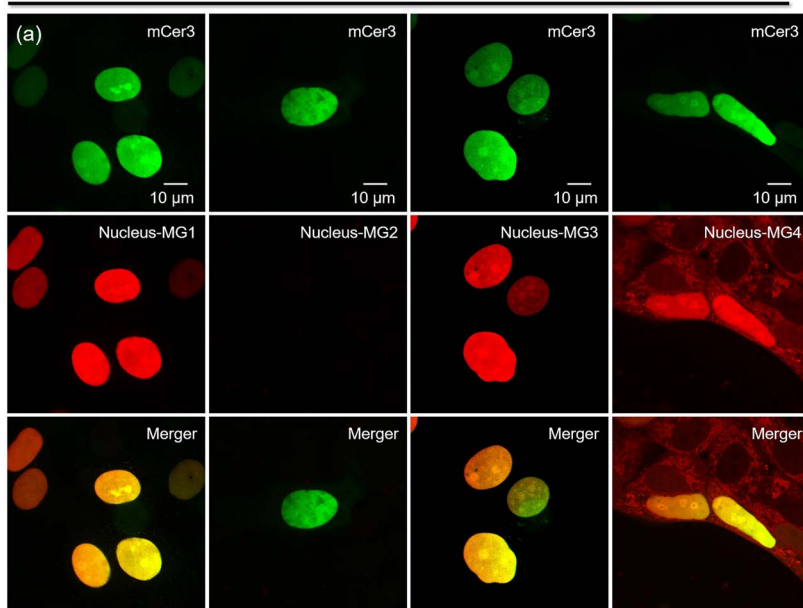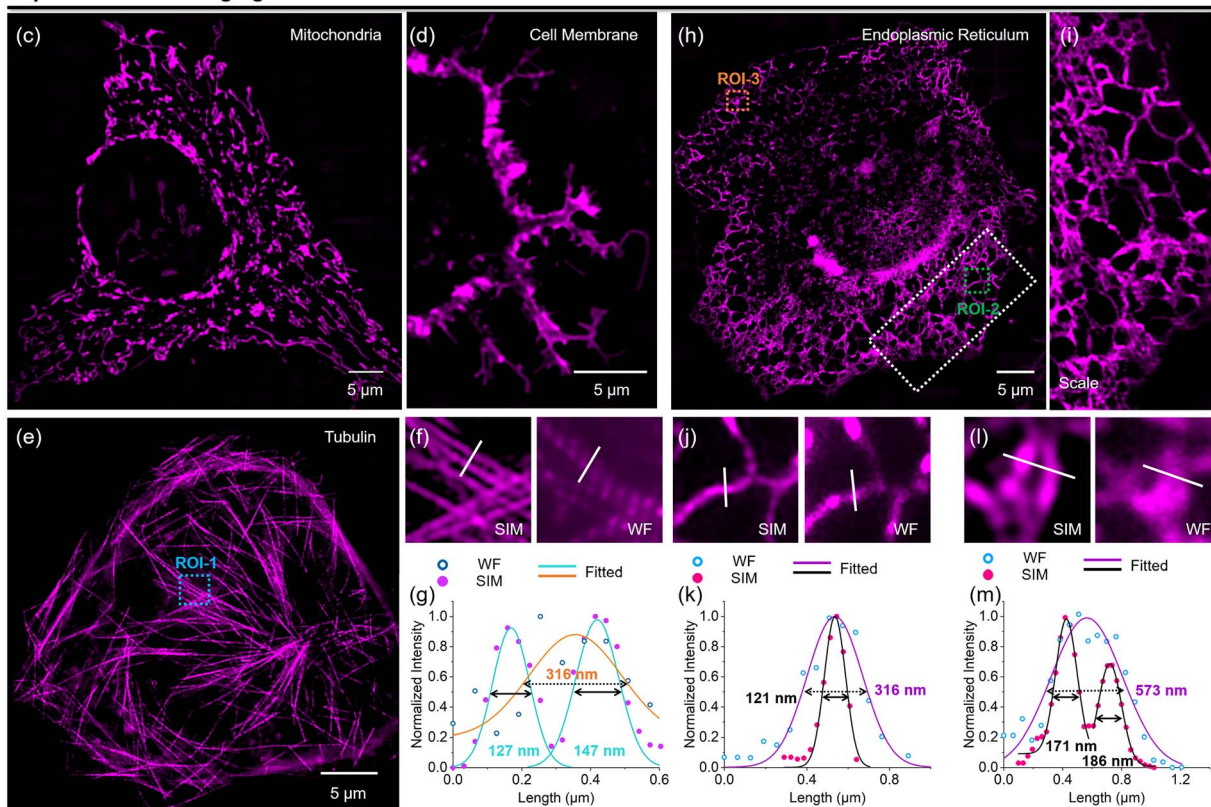

Fig. 4 (a) Confocal images of HeLa cells expressing dL5**-mCer3 in the nucleus with **MG1–4**. (b) Confocal images of HeLa cells expressing dL5**-mCer3 in mitochondria and ER with the addition of 200 nM **MG3**. Green fluorescence signals from mCer3; red fluorescence signals from **MG**/dL5**. SIM imaging of mitochondria (c), cell membrane (d), tubulin (e) and endoplasmic reticulum (h). (i) Enlarged view of ROI-2 in (h). (f) SIM and widefield of ROI-1 in (e). (g) Intensity distributions across tubulin (white line) in (f). SIM and widefield of ROI-2 (j) and ROI-3 (l) in (h). (k) and (m) Intensity distributions across ER (white line) in (j) and (l).

methyl carbons of **MG1** contributed approximately half of the total contact in the **MG1**-L5* homodimer.[35] Therefore, the absence of alkyl groups on the nitrogen atoms of **MG2** might allow free rotation of the aromatic rings within the binding cavity, resulting in fluorescence quenching and underscoring the significance of the azetidine group.

Briefly, we successfully enhanced the brightness ($\varepsilon \times \varphi$) of the **MG1**/dL5** fluoromodule by 2.6-fold by replacing the dimethylamino group with a four-membered azetidine ring. While the affinity of **MG3** for dL5** was lower than that of **MG1**, its K_d value of 16 nM was comparable to previous reports and sufficient for fluorescence imaging.[21] Notably, **MG3** exhibited a substantial absorbance increase of 2.6-fold, compared to a 1.4-fold increase in **MG1**, thereby enhancing its fluorogenicity. Additionally, the absorption maximum of the **MG3**/dL5** complex at 639 nm aligns well with the standard 640 nm laser used in fluorescence imaging.

With the enhanced **MG3**/dL5** fluoromodule, excellent biocompatibility and high stability (Fig. S5 and S6†), we further explored its application in fluorescence imaging. **MG3** demonstrates rapid penetration into cells, with the cellular uptake of **MG3** primarily mediated by clathrin-dependent endocytosis (Fig. S7†). Using a myc-dL5**-mCer3 fusion protein, we assessed the fluorescence activation capability of this fluoromodule in live cells (Fig. 4a). Similar to the *in vitro* responses, **MG2** showed negligible fluorescence signals in the nucleus, and **MG4** exhibited a high background fluorescence. In contrast, **MG3** demonstrated excellent fluorogenicity compared to **MG1**, establishing it as a superior fluorogen-activating protein probe for live-cell imaging. We selected mitochondria and the endoplasmic reticulum as representative organelles for labeling and imaging with **MG3**. Plasmids containing dL5**, the fluorescent protein mCer3, and a subcellular targeting sequence were transfected into HeLa cells, followed by the addition of 200 nM **MG3**. As shown in Fig. 4b, **MG3** (red) colocalized with mCer3 (green) in the two organelles, indicating that dL5** was appropriately expressed in various subcellular environments, effectively activating the fluorescence of **MG3**.

To demonstrate the capabilities of **MG3** in super-resolution imaging, we first employed SIM to visualize various cellular structures (Fig. 4c–i), including mitochondria, cell membrane, microtubules, and endoplasmic reticulum (ER). **MG3** effectively resolved the intricate structures of these organelles at the nanoscale. Adjacent microtubules that appeared indistinguishable under widefield were clearly discernible through super-resolution images, achieving resolutions of 127 nm and 147 nm (Fig. 4f and g). Furthermore, **MG3** allowed for the visualization of the fine meshwork of ER, revealing an ER tubule width of 121 nm compared to a width of 316 nm observed with widefield imaging (Fig. 4j and k), further showcasing the high fluorogenicity and brightness of our probes. While widefield identified an ER tubule at 573 nm, super-resolution imaging revealed the finer structural details of the ER mesh, highlighting **MG3**'s substantial potential for super-resolution applications.

Previous reports have indicated that **MG1**/dL5** is a highly photostable fluoromodule, making it suitable for super-
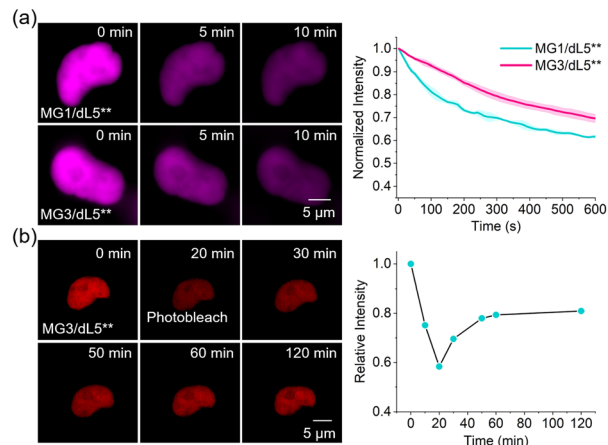

Fig. 5 (a) Quantification of the relative fluorescent intensity of **MG1**/dL5** and **MG3**/dL5** in HeLa cells with continuous irradiation using super-resolution SIM microscopy. (b) Fluorescence recovery of **MG3**/dL5** in HeLa cells after 20 min of continuous irradiation using a 640 nm laser.

resolution imaging of diverse cellular structures.[24] Here, we further evaluated the photostability of both **MG1**/dL5** and **MG3**/dL5** in fixed cells under continuous 640 nm laser irradiation during SIM microscopy (Fig. 5). The fluorescence intensity of **MG3**/dL5** remained at 70% after 600 s, which is slightly higher than the 62% observed for **MG1**/dL5** (Fig. 5a). These findings were consistent with the outcomes of our confocal microscopy analysis (Fig. S8–S10†). We attribute the enhanced photostability of **MG3**/dL5** to the buffering effect of **MG3** within the fluoromodules. As illustrated in Fig. 5b, continuous irradiation with the 640 nm laser reduced the fluorescence of **MG3**/dL5** to 58%. Upon cessation of the laser exposure, the fluorescence gradually recovered to 80% after 40 min. This recovery is likely due to the reduced affinity of dL5** for **MG3**, allowing fresh dyes to replenish those that were photobleached, a mechanism similar to the buffering observed in our previously reported fluorogenic probes.[25–29]

Due to its enhanced photostability, we applied **MG3**/dL5** for long-term tracking of mitochondrial dynamics through super-resolution imaging. The mitochondrial network was clearly identified under SIM. As shown in Fig. 6a and Movie S1,† we monitored mitochondrial fission over a 30-minute tracking period. At 9 min, the mitochondrion marked by a green arrow gradually extended to establish contact with a neighboring mitochondrion. This contact point underwent continuous changes over the next 10 minutes. Notably, significant deformation of the neighboring mitochondrion was observed at 16 min. By 22 min, the mitochondrion indicated by the green arrow exhibited a boundary and began to produce a small daughter mitochondrion. Subsequently, the mitochondrion marked by the green arrow remained in contact with the daughter mitochondrion, eventually leading to complete separation from the original mitochondrion. Additionally, multiple fission and contact events were recorded in the same region, highlighted by green arrows. Mitochondrial autophagy is also documented in Fig. 6b and Movie S2.† The mitochondrion
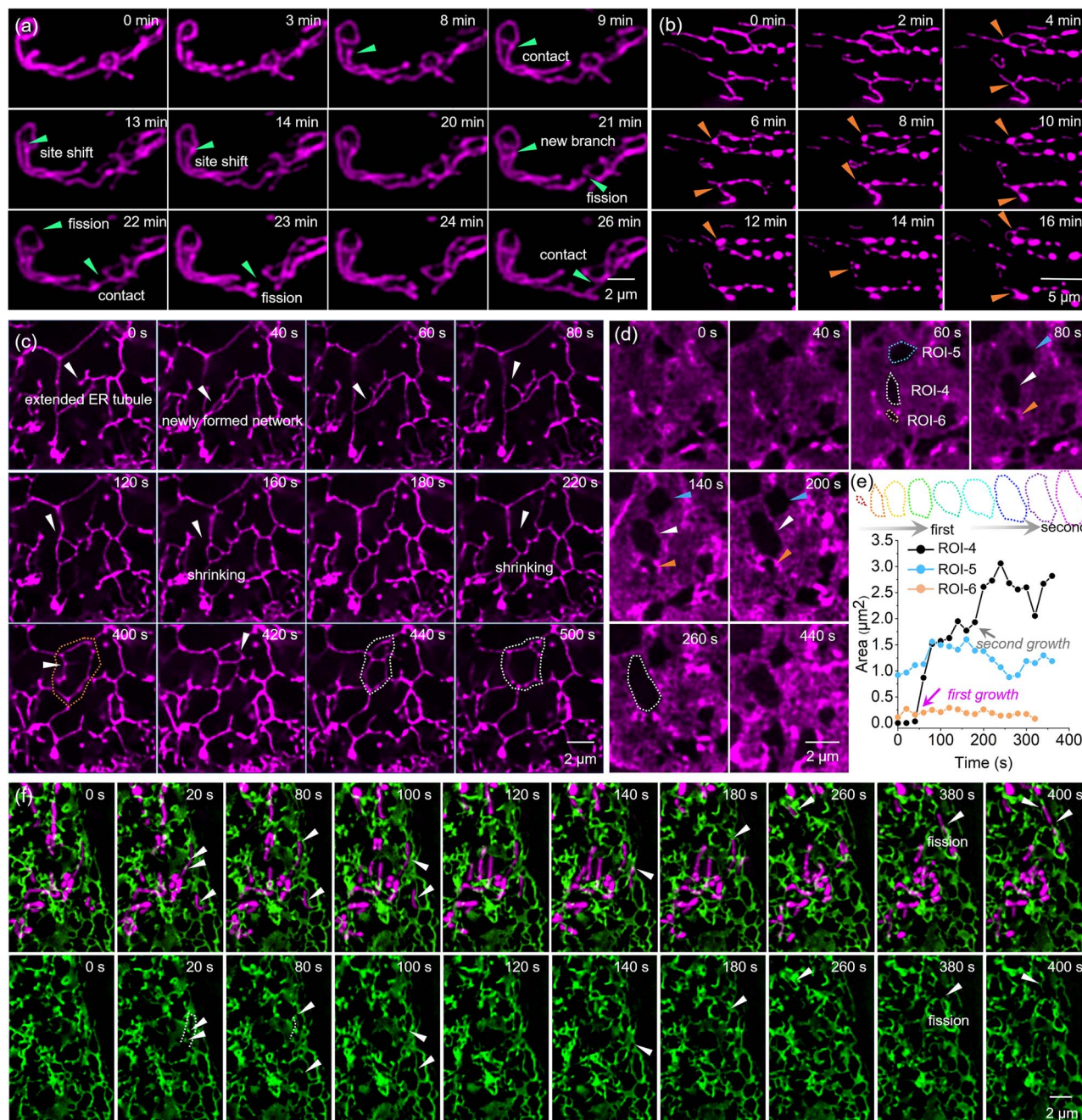
Fig. 6 Time-lapse SIM images of (a) mitochondrial fission, (b) mitophagy, ER tubule (c) and RER dynamics (d) in living HeLa cells through **MG3/dL5**** labeling. (e) Time colored outline of the cavity in ROI-4. And the time dependence of area in ROI-4-6. (f) Dual-color time-lapse SIM images of mitochondria and ER with **MG3/dL5**** and GFP in living HeLa cells.

marked by an orange arrow gradually swelled at the bifurcation point, transitioning from a slender linear shape to a spherical morphology at 8 minutes.

Using **MG3**, we also visualized the dynamic behavior of the ER, including the movement of ER tubules and the formation and disruption of ER networks (Fig. 6c). At 0 s, an ER tubule, marked by a white arrow, gradually extended and formed a new network by 40 seconds. This network subsequently gave rise to a new ER tubule, also indicated by a white arrow, at 80 s, which rapidly moved to form a triangular network by 120 s. The newly

formed network exhibited significant dynamics and was not stable, gradually shrinking between 120 and 180 s and ultimately breakingoken apart at 220 s. By 400 s, a new budding point appeared in the same area (marked by a white arrow) and created a new network by 420 s, which divided the original network (outlined by an orange dotted frame) into two smaller networks. In contrast to the previous observation, the upper network gradually shrank while the lower network expanded, ultimately forming a larger network by 500 s.

Additionally, we observed a cell rich in rough endoplasmic reticulum (Fig. S11†) and monitored the formation and morphological changes of hollow regions within the rough endoplasmic reticulum (Fig. 6d). We selected three regions of interest (ROIs) – ROI-4, ROI-5, and ROI-6 – to examine the cavities, which exhibited different dynamic behaviors. The mature cavity in ROI-4 showed rapid growth after 60 s, followed by fluctuations in size, with a gradual reduction occurring between 160 and 260 s (Fig. 6e). Notably, newly formed cavities in ROI-5 displayed two distinct growth phases (Fig. 6e). The outline of cavity was marked with a colored dotted frame and the area was recorded. The first occurred in the initial formation period from 40 to 60 s, during which the cavity area increased from 0.03 μm^2 to 1.52 μm^2. The second significant growth phase was observed between 160 and 240 s, where the area expanded from 1.77 μm^2 to 3.06 μm. This suggested that the expansion of cavities formed within the rough endoplasmic reticulum might involve multiple short-term phases of growth rather than a uniform slow process.

Moreover, we achieved dual-color super-resolution imaging of the ER and mitochondria using **MG3**, enabling us to monitor the movement of mitochondria being pulled by the ER (Fig. 6f).

At 20 s, a mitochondrion marked by a white arrow was completely enveloped by the green ER, showing stronger fluorescence at the contact sites. This phenomenon was similarly observed at 80 and 100 s. Furthermore, by 80 s, the mitochondrion, which was closely apposed to the ER, exhibited a curved morphology (indicated by a dotted line), reflecting strong interactions. At 140 s, the mitochondrion marked by a white arrow displayed high dynamics, being pulled upward by ER–mitochondria contact sites, leading to division at 380 s, during which the ER participated in this fission event. Notably, ER–mitochondria contact sites were found to define the positions of mitochondrial fission, and ER–mitochondria contacts were maintained throughout the entire division process, with the two compartments bounded by the ER tubule moving back and forth.

Conclusions

In summary, we have enhanced the brightness of the MG/dL5** fluoromodule by replacing the N,N-dimethylamino group in MG with an azetidine structure to suppress the TICT effect. Our probe, **MG3**, demonstrated a quantum yield of 0.28 in the presence of dL5**, significantly higher than that of the conventional **MG1**, which showed a quantum yield of 0.12. This modification results in a 2.6-fold brightness enhancement over **MG1**. Additionally, the optimized **MG3**/dL5** complex exhibits advantages in fluorogenicity, photostability, and absorption maximum, making it an ideal fluoromodule for live-cell and super-resolution imaging. The enhanced buffering capacity of **MG3** allows for reversible binding with the FAP, enabling free fluorogen molecules to replace those that have been photobleached at the target site. This characteristic supports stable fluorescence over time, facilitating continuous dynamic imaging of various cellular structures.

Data availability

All data are available in the main text and the ESI† or available from the authors upon reasonable request.

Author contributions

Fei Deng: conceptualization, investigation, analysis, writing – original draft. Xiangning Fang: investigation, analysis. Qinglong Qiao: conceptualization, investigation, analysis, writing – original draft. Lu Miao: investigation, analysis. Shuangshuang Long: investigation, analysis. Zhaochao Xu: conceptualization, supervision, writing – reviewing & editing, funding acquisition.

Conflicts of interest

There are no conflicts to declare.

Acknowledgements

Notes and references

1 T. A. Daugird, Y. Shi, K. L. Holland, H. Rostamian, Z. Liu, L. D. Lavis, J. Rodriguez, B. D. Strahl and W. R. Legant, Correlative single molecule lattice light sheet imaging reveals the dynamic relationship between nucleosomes and the local chromatin environment, *Nat. Commun.*, 2024, **15**, 4178.

2 Q. Qiao, W. Liu, Y. Zhang, J. Chen, G. Wang, Y. Tao, L. Miao, W. Jiang, K. An and Z. Xu, In Situ Real-Time Nanoscale Resolution of Structural Evolution and Dynamics of Fluorescent Self-Assemblies by Super-Resolution Imaging, *Angew. Chem., Int. Ed.*, 2022, **134**, e202208678.

3 L. Miao, C. Yan, Y. Chen, W. Zhou, X. Zhou, Q. Qiao and Z. Xu, SIM imaging resolves endocytosis of SARS-CoV-2 spike RBD in living cells, *Cell Chem. Biol.*, 2023, **30**, 248–260.

4 S. Samanta, K. Lai, F. Wu, Y. Liu, S. Cai, X. Yang, J. Qu and Z. Yang, Xanthene, cyanine, oxazine and BODIPY: the four pillars of the fluorophore empire for super-resolution bioimaging, *Chem. Soc. Rev.*, 2023, **52**, 7197–7261.

5 E. Kozma and P. Kele, Fluorogenic probes for super-resolution microscopy, *Org. Biomol. Chem.*, 2019, **17**, 215–233.

6 J. Kwon, M. S. Elgawish and S. H. Shim, Bleaching-Resistant Super-Resolution Fluorescence Microscopy, *Adv. Sci.*, 2022, **9**, 2101817.

7 F. M. Jradi and L. D. Lavis, Chemistry of photosensitive fluorophores for single-molecule localization microscopy, *ACS Chem. Biol.*, 2019, **14**, 1077–1090.

8 Q. Qiao, W. Liu, W. Chi, J. Chen, W. Zhou, N. Xu, J. Li, X. Fang, Y. Tao and Y. Zhang, Modulation of dynamic aggregation in fluorogenic SNAP-tag probes for long-term super-resolution imaging, *Aggregate*, 2023, **4**, e258.

9 A. Salam, K. Kaushik, B. Mukherjee, F. Anjum, G. T. Sapkal, S. Sharma, R. Garg and C. K. Nandi, A zinc metal complex as an NIR emissive probe for real-time dynamics and in vivo embryogenic evolution of lysosomes using super-resolution microscopy, *Chem. Sci.*, 2024, **15**, 15659–15669.

10 Z.-H. Wu, X. Zhu, Q. Yang, Y. Zagranyarski, K. Mishra, H. Strickfaden, R. P. Wong, T. Basché, K. Koynov and M. Bonn, Near-infrared perylenecarboximide fluorophores for live-cell super-resolution imaging, *J. Am. Chem. Soc.*, 2024, **146**, 7135–7139.

11 X. Ren, C. Wang, X. Wu, M. Rong, R. Huang, Q. Liang, T. Shen, H. Sun, R. Zhang and Z. Zhang, Auxochrome dimethyl-dihydroacridine improves fluorophores for prolonged live-cell super-resolution imaging, *J. Am. Chem. Soc.*, 2024, **146**, 6566–6579.

12 Q. Qiao, A. Song, K. An, N. Xu, W. Jia, Y. Ruan, P. Bao, Y. Tao, Y. Zhang and X. Wang, Spontaneously Blinkogenic Probe for Wash-Free Single-Molecule Localization-Based Super-Resolution Imaging in Living Cells, *Angew. Chem., Int. Ed.*, 2025, **64**, e202417469.

13 Q. Qiao, W. Liu, J. Chen, X. Wu, F. Deng, X. Fang, N. Xu, W. Zhou, S. Wu and W. Yin, An Acid-Regulated Self-Blinking Fluorescent Probe for Resolving Whole-Cell Lysosomes with Long-Term Nanoscopy, *Angew. Chem., Int. Ed.*, 2022, **134**, e202202961.

14 M. Minoshima, S. I. Reja, R. Hashimoto, K. Iijima and K. Kikuchi, Hybrid Small-Molecule/Protein Fluorescent Probes, *Chem. Rev.*, 2024, **124**, 6198–6270.

15 E. Gallo, Fluorogen-activating proteins: Next-generation fluorescence probes for biological research, *Bioconjugate Chem.*, 2019, **31**, 16–27.

16 L. A. Perkins and M. P. Bruchez, Fluorogen activating protein toolset for protein trafficking measurements, *Traffic*, 2020, **21**, 333–348.

17 S. Xu and H.-Y. Hu, Fluorogen-activating proteins: beyond classical fluorescent proteins, *Acta Pharm. Sin. B*, 2018, **8**, 339–348.

18 Y. Zhang, W. Zhou, N. Xu, G. Wang, J. Li, K. An, W. Jiang, X. Zhou, Q. Qiao and X. Jiang, Aniline as a TICT rotor to derive methine fluorogens for biomolecules: A curcuminoid-BF2 compound for lighting up HSA/BSA, *Chin. Chem. Lett.*, 2023, **34**, 107472.

19 C. Szent-Gyorgyi, B. A. Schmidt, Y. Creeger, G. W. Fisher, K. L. Zakel, S. Adler, J. A. J. Fitzpatrick, C. A. Woolford, Q. Yan, K. V. Vasilev, P. B. Berget, M. P. Bruchez, J. W. Jarvik and A. Waggoner, Fluorogen-activating single-chain antibodies for imaging cell surface proteins, *Nat. Biotechnol.*, 2008, **26**, 235–240.

20 M. Zhang, S. K. Chakraborty, P. Sampath, J. J. Rojas, W. Hou, S. Saurabh, S. H. Thorne, M. P. Bruchez and A. S. Waggoner, Fluoromodule-based reporter/probes designed for in vivo fluorescence imaging, *J. Clin. Invest.*, 2015, **125**, 3915–3927.

21 C. P. Pratt, J. J. He, Y. Wang, A. L. Barth and M. P. Bruchez, Fluorogenic Green-Inside Red-Outside (GIRO) Labeling Approach Reveals Adenylyl Cyclase-Dependent Control of BK alpha Surface Expression, *Bioconjugate Chem.*, 2015, **26**, 1963–1971.

22 Q. Zhang, Q. Wang, Y. Sun, L. Zuo, V. Fetz and H.-Y. Hu, Superior Fluorogen-Activating Protein Probes Based on 3-Indole–Malachite Green, *Org. Lett.*, 2017, **19**, 4496–4499.

23 J. A. Fitzpatrick, Q. Yan, J. J. Sieber, M. Dyba, U. Schwarz, C. Szent-Gyorgyi, C. A. Woolford, P. B. Berget, A. S. Waggoner and M. P. Bruchez, STED nanoscopy in living cells using fluorogen activating proteins, *Bioconjugate Chem.*, 2009, **20**, 1843–1847.

24 S. Saurabh, A. M. Perez, C. J. Comerci, L. Shapiro and W. Moerner, Super-resolution imaging of live bacteria cells using a genetically directed, highly photostable fluoromodule, *J. Am. Chem. Soc.*, 2016, **138**, 10398–10401.

25 J. Chen, C. Wang, W. Liu, Q. Qiao, H. Qi, W. Zhou, N. Xu, J. Li, H. Piao and D. Tan, Stable Super-Resolution Imaging of Lipid Droplet Dynamics through a Buffer Strategy with a Hydrogen-Bond Sensitive Fluorogenic Probe, *Angew. Chem., Int. Ed.*, 2021, **133**, 25308–25317.

26 N. Xu, Q. Qiao, X. Fang, G. Wang, K. An, W. Jiang, J. Li and Z. Xu, Solvatochromic Buffering Fluorescent Probe Resolves the Lipid Transport and Morphological Changes during Lipid Droplet Fusion by Super-Resolution Imaging, *Anal. Chem.*, 2024, **96**, 4709–4715.

27 W. Zhou, Y. Tao, Q. Qiao, N. Xu, J. Li, G. Wang, X. Fang, J. Chen, W. Liu and Z. Xu, Cell-Impermeable Buffering Fluorogenic Probes for Live-Cell Super-Resolution Imaging of Plasma Membrane Morphology Dynamics, *ACS Sens.*, 2024, **9**, 3170–3177.

28 K. An, Q. Qiao, W. Zhou, W. Jiang, J. Li and Z. Xu, Stable Super-Resolution Imaging of Cell Membrane Nanoscale Subcompartment Dynamics with a Buffering Cyanine Dye, *Anal. Chem.*, 2024, **96**, 5985–5991.

29 W. Jiang, Q. Qiao, J. Chen, P. Bao, Y. Tao, Y. Zhang and Z. Xu, Rna Buffering Fluorogenic Probe for Nucleolar Morphology Stable Imaging And Nucleolar Stress-Generating Agents Screening, *Adv. Sci.*, 2024, **11**, 2309743.

30 L. Wang, W. Du, Z. Hu, K. Uvdal, L. Li and W. Huang, Hybrid rhodamine fluorophores in the visible/NIR region for biological imaging, *Angew. Chem., Int. Ed.*, 2019, **58**, 14026–14043.

31 X. Liu, Q. Qiao, W. Tian, W. Liu, J. Chen, M. J. Lang and Z. Xu, Aziridinyl Fluorophores Demonstrate Bright Fluorescence and Superior Photostability by Effectively Inhibiting Twisted Intramolecular Charge Transfer, *J. Am. Chem. Soc.*, 2016, **138**, 6960–6963.

32 A. N. Butkevich, M. L. Bossi, G. v. Lukinavičius and S. W. Hell, Triarylmethane fluorophores resistant to oxidative photobluing, *J. Am. Chem. Soc.*, 2018, **141**, 981–989.

33 W. Zhou, X. Fang, Q. Qiao, W. Jiang, Y. Zhang and Z. Xu, Quantitative assessment of rhodamine spectra, *Chin. Chem. Lett.*, 2021, **32**, 943–946.

34 J. B. Grimm, B. P. English, J. J. Chen, J. P. Slaughter, Z. J. Zhang, A. Revyakin, R. Patel, J. J. Macklin,

D. Normanno, R. H. Singer, T. Lionnet and L. D. Lavis, A general method to improve fluorophores for live-cell and single-molecule microscopy, *Nat. Methods*, 2015, **12**, 244–250.

35 C. Szent-Gyorgyi, R. L. Stanfield, S. Andreko, A. Dempsey, M. Ahmed, S. Capek, A. S. Waggoner, I. A. Wilson and M. P. Bruchez, Malachite Green Mediates Homodimerization of Antibody V-L Domains to Form a Fluorescent Ternary Complex with Singular Symmetric Interfaces, *J. Mol. Biol.*, 2013, **425**, 4595–4613.

36 J. J. He, Y. Wang, M. A. Missinato, E. Onuoha, L. A. Perkins, S. C. Watkins, C. M. St Croix, M. Tsang and M. P. Bruchez, A genetically targetable near-infrared photosensitizer, *Nat. Methods*, 2016, **13**, 263–268.